Experimental estimation of turbulence modulation in droplet-laden two-phase jet

Hao Wu [1,2] Zhenyu Zhang [1,*] Fujun Zhang,[1] Kun Wu,[3] and William L. Roberts[2]
[1]*School of Mechanical Engineering, Beijing Institute of Technology, Beijing 100081, China*
[2]*Clean Combustion Research Center, King Abdullah University of Science and Technology, Thuwal, Saudi Arabia*
[3]*State Key Laboratory of High Temperature Gas Dynamics, Institute of Mechanics, Chinese Academy of Sciences, Beijing 100190, China*

(Received 16 March 2023; accepted 14 August 2023; published 5 September 2023)

The effect of liquid droplets generated from air-assisted atomization on gas flow characteristics was studied experimentally. A phase/Doppler particle analyzer was used to measure velocity and size distributions of continuous and dispersed phases in the droplet-laden two-phase flow. A comparison of mean gas velocity with and without droplets indicates the expected influence of dispersed phase on the carrier phase, i.e., two-way coupling. The flow characterization result shows the presence of liquid droplets contributes to the increase of gas-phase flow velocity in the spray field. The effect of liquid droplets on gas-phase turbulence is manifested in three ways. First, the presence of droplets leads to the increase in fluctuation velocity of gas-phase flow. Subsequently, it is observed that the range of fluctuation velocities in the gas phase is expanded in two-phase flow compared with single-phase flow. In the region characterized by a steep velocity gradient, the initial gas fluctuation velocities in two-phase flow demonstrate a notable enhancement of 20% compared with single-phase flow. Furthermore, the presence of droplets induces axial stretching within the shear region of the gas phase, and this stretching effect is particularly pronounced in cases of higher fuel-injection durations, primarily due to the influence of droplet gravity. The data obtained from the analysis of velocity gradient and fluctuation velocity within the two-phase flow field reveal a distinct segmental linear relationship, deviating from previous findings reported in the literature and highlighting a deeper understanding of the underlying mechanisms in current two-phase flow systems.

DOI: 10.1103/PhysRevFluids.8.094301

I. INTRODUCTION

Turbulent two-phase flow occurs in many natural, chemical, and industrial processes, e.g., rain formation, liquid-liquid emulsion, and spray atomization in combustors [1]. Turbulent flows laden with liquid droplets or solid particles are known as members of turbulent dispersed multiphase flows (TDMFs) [2]. When the gas phase is continuous, the actual flow can be divided into particle- and droplet-laden flows according to the type of discrete phase. Comprehensive reviews can be found

*Corresponding author: zhenyu.zhang@bit.edu.cn

in Refs. [3,4]. In this case, the gas phase (continuous phase) is usually considered the carrier phase, while the particles/droplets (discrete phase) are considered the dispersed phase. The interaction of dispersed phase and turbulence leads to changes in the level of the gas-phase turbulence intensity. The presence of a particle/droplet cloud generally has two opposite effects on the turbulence status of the carrier flow, that is, either augmentation or attenuation [5].

The turbulence modulation is determined by multiple factors. Balachandar and Eaton [3] summarized that turbulence modulation in a dilute suspension is attributed to three main mechanisms: (a) enhanced dissipation due to the presence of particles, (b) the transfer of kinetic energy to the fluid from the particles, and (c) the formation of wakes and vortex shedding behind the particles. Gai *et al.* [5] reviewed the studies related to turbulence modulation and highlighted the main inducing factors of turbulence modulation including the disruption of velocity gradient and streamline curvature in the continuous phase, particle vortex shedding, and the decay of particle-induced drag force. Currently, the factors that are widely recognized as having a significant influence on turbulence modulation include particle size [6–10], particle Reynolds number [8,11], particle Stokes number [12–16], mass loading [17–19], and volume fraction [20]. These factors have different effects on various practical flow scenarios, such as pipe flow, channel flow, and jets. In some cases, their impacts may even contradict each other, and our understanding of these phenomena remains limited [19].

Particle image velocimetry [21,22], laser Doppler anemometry [23,24], phase Doppler particle analyzer (PDPA) analysis [25], and high-speed visualization are the commonly used experimental methods for gas-particle turbulent flow investigation. For the effect of particle size, it is generally believed that fine particles weaken the gas-phase turbulence intensity, while large particles enhance the turbulence intensity [25–29]. When the situation comes to medium-sized particles, gas-phase turbulence intensity is determined by the particle position in the flow field. Gore and Crowe [7] provided a systematic summary of previous experimental results, including jet flow, pipe flow, gas-particle flow, and gas-liquid flow. The results show that small particle ($D_p < 200\,\mu$m) scales tend to cause turbulence attenuation, while large particles ($D_p > 200\,\mu$m) tend to enhance turbulence. However, some exceptions have been found in some jet flows, where fine particles have been reported to enhance gas-phase turbulence [9,10]. Elghobashi and Truesdell [6] proposed a length-scale ratio based on D_p/η and used it to analyze the effect of particles on turbulence modulation. When D_p/η is $\ll 1$, the effect of particles on the turbulence of the carrier flow is small.

Regarding the effect of the particle Reynolds number, Paris [8] experimentally studied a vertical fully developed channel flow with particles smaller than Kolmogorov length scale η. The results indicated that the mass-loading ratio increases the effect of turbulence attenuation at low particle Reynolds numbers Re_p, as defined by

$$\mathrm{Re}_p = \frac{(\rho_p - \rho_f)|u_f - u_p|d_p}{\mu_f}, \tag{1}$$

where ρ is the mass density, u is the velocity, and d_p denotes the diameter. The subscripts p and f represent particles and fluids, respectively. Hetsroni [11] showed that particles extract energy from the flow and dissipate it if the particle Reynolds number is <110. When the Reynolds number of particles is >400, it will lead to vortex instability and shedding, thus enhancing turbulence. Clift *et al.* [30] concluded that, in particle-laden flow, particle wake instability occurs when the particle Reynolds number is ~ 130, while vortex shedding occurs when the particle Reynolds number is ~ 270.

The experimental results of Hetsroni and Sokolov [13] show a decrease of turbulence intensities in the two-phase jet compared with the single-phase jet when the particle Stokes number (Stk) is <1. After that, Ferrante and Elghobashi [12] also used the particle Stokes number to characterize the turbulence modulation. The results show that, when the particle Stokes number is $\ll 1$, the viscous dissipation is greater than the case of turbulent flow without particles. When the particle Stokes number is >1, the turbulent length and time scale grow faster. In the case of $\mathrm{Stk} \approx 1$,

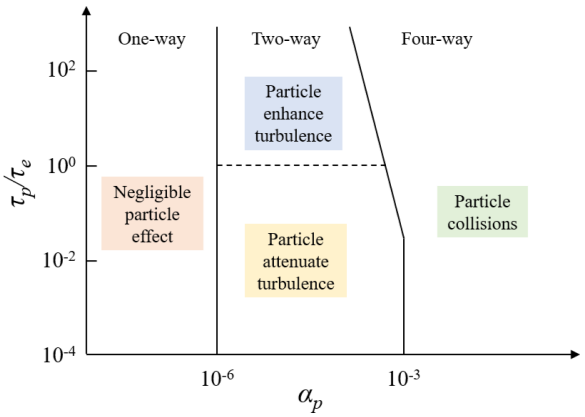

FIG. 1. Different regimes of interaction between particles and turbulence [20].

the turbulent kinetic energy dissipation rate increases while the turbulent intensity decreases. Kulick *et al.* [23] conducted an experimental study of fully developed turbulent channel flows where the particle size is smaller than the Kolmogorov length scale η. The results show that the increase of the particle Stokes number and mass loading leads to an attenuation of the turbulence, and the reduction in turbulence intensity in the crossflow direction is significantly larger than that in the stream-wise direction. However, Tanaka and Eaton [15] and Luo *et al.* [14] found that the Stokes number is not the most important parameter causing the turbulent modulation because attenuation of the turbulence can be found when Stk < 60.

Eaton [18] proposed that turbulence modulation is more sensitive to the effect of mass loading rather than the particle response. Additionally, Liu *et al.* [19] consider turbulence modulation to be determined by a group of parameters rather than a single one, i.e., a combination of swirling number, mass loading, particle size, and density, where mass loading should be the leading order. In addition, Yamamoto *et al.* [31] showed that interparticle interactions and particle-wall interactions contribute significantly to turbulence attenuation. Elghobashi [20] provided an intuitive result for the effect of the volume fraction α_p on turbulence modulation, as shown in Fig. 1. Here, τ_P represents the response time of the particle, and τ_e is the turnover time scale of the large-scale vortex and is defined as the ratio of the turbulence length scale to the root mean square (rms) of the fluctuation velocity. There are three different turbulence modulation mechanisms for different particle volume fractions. When $\alpha_p < 10^{-6}$, it is difficult for the particles to have a substantial effect on the turbulence, so the coupling between the two phases is mainly one-way coupling. When the volume fraction of particles is between 10^{-6} and 10^{-3}, the number of particles starts to affect the turbulence in the continuous phase. Turbulence enhancement and turbulence weakening can be distinguished according to the scale ratio of the particles to the turbulent structure. When the volume fraction of particles is $>10^{-3}$, the interaction between particles, especially particle collision and coalescence, will have a nonnegligible effect on the turbulence, and the particles and turbulence will be coupled in a four-way regime.

Authors of previous studies, both numerical and experimental, on turbulence modulation of TDMF have predominantly focused on solid particles [32]. In contrast, there has been relatively scarce exploration regarding the effect of liquid droplets on gas turbulence due to the inherent complexity of the phenomenon. In comparison with solid particles, droplets in turbulent flows may undergo some additional physical processes, i.e., evaporation, deformation, coalescence, and even internal fluid circulation.

The study of evaporating droplets involves the analysis of various physical phenomena experienced by solid particles as well as additional intricacies. These complexities arise from the interaction of evaporating droplets with the surrounding carrier phase, involving mass and

thermal energy transfer. The rate of evaporation and subsequently the droplet size are intricately linked to the local flow characteristics, leading to significant temporal and spatial variations in the lifespan of the droplet [33]. Therefore, the presence of evaporating droplets gives rise to polydisperse flows, characterized by distinctive preferential concentrations and flow modulations that are anticipated to deviate significantly from those observed for solid particles [34]. In addition, when turbulent gas flows through a stationary droplet, a velocity gradient is formed around the droplet, causing a nonuniform distribution of pressure. The continuous phase exerts external forces on the droplet, resulting in deformation. If these external forces surpass the internal forces and stresses that maintain the integrity of the droplet, the droplet undergoes a breakup process. To accurately predict the deformation of the interface between the dispersed and continuous phases, it is essential to appropriately incorporate the influences of surface tension as well as the disparate viscosities and densities of the two phases into the governing equations of motion [2].

Hetsroni and Sokolov [13] carried out earlier and extensive experimental investigations of the effect of injected oil droplets on the turbulent structure of gas-phase jets. They found that the presence of the dispersed phase reduced the spectral intensity, especially at higher frequencies. Additionally, this modulating effect was found to increase with the concentration of the dispersed phase. In a recent study, Shinjo *et al.* [35] examined the impact of finite-sized droplets/ligaments on turbulence modulation and scalar mixing within a dense fuel spray using a direct numerical simulation (DNS) dataset. The findings revealed a universal feature of isotropic turbulence within a region characterized by a relatively low droplet number density. However, the presence of droplets resulted in slight modifications to the alignment of strain eigenvectors with vorticity and the mixture fraction gradient. Additionally, the results of numerical simulations from Dodd and Ferrante [36] show that increasing droplet Weber number (based on the rms velocity of turbulence), droplet- to carrier-fluid density ratio, and droplet- to carrier-fluid viscosity ratio lead to the increase of the decay rate of the two-fluid turbulence kinetic energy. The droplets enhance the dissipation rate of turbulence kinetic energy (TKE) by enhancing the local velocity gradients near the droplet interface. Rosa *et al.* [37] investigated the effect of two-way momentum coupling on the collision coalescence of water droplets, which have been examined using the combined Eulerian-Lagrangian numerical approach. They found that the effect of two-way coupling is significant for both droplet clustering and the radial relative velocity. Gai *et al.* [38] conducted a numerical study to examine the turbulence generated by industrial spray nozzles. Their findings revealed that the turbulent kinetic energy is predominantly concentrated within the spray cone and diminishes rapidly as the vertical distance from the nozzle increases. Moreover, the spray droplet diameter was found to have a significant impact on the turbulent kinetic energy. Water sprays produced by these industrial nozzles can generate highly intense turbulence in the immediate vicinity of the nozzle, with the intensity gradually decreasing as the distance from the nozzle increases. In addition, a detailed review focusing on DNSs of turbulent flows laden with droplets or bubbles can be found in Ref. [2]. Based on these studies, it is evident that research on turbulence modulation caused by droplets predominantly relies on numerical computations. Experimental assessments of the turbulent modulation induced by spray droplets are sparsely documented in the existing literature.

Air-assisted sprays, as a form of twin-fluid atomization, facilitate improved atomization by incorporating additional pressurized gas flow/stream (typically air) to enhance the destabilization of the jet or spray and promote the breakup of the liquid [39]. During this process, the kinetic energy of high-velocity flowing airstream and the presence of intense shear stresses near the gas-liquid interface are effectively utilized to shatter the liquid jet/sheet into ligaments, which subsequently undergo further disintegration, transforming into dispersed droplets under a relatively low pressure compared with the single-fluid pressure atomization method [40]. On the other hand, air-assisted sprays are characterized by inherently complicated multiple atomization regimes and gas-liquid two-phase flow behaviors [41]. In the region of the spray/flow field located far from the nozzle, the fully atomized spray transforms into a droplet-laden jet/flow with intense gas-liquid interaction.

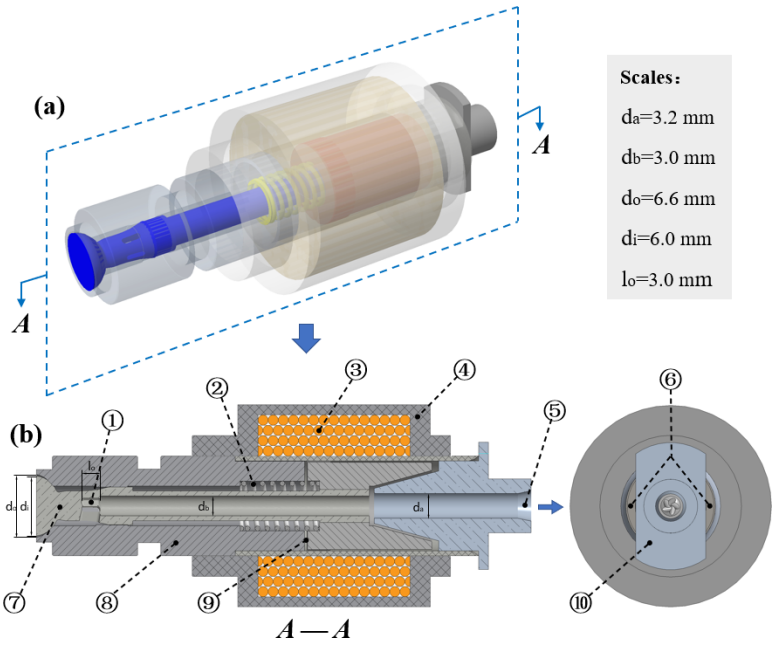

FIG. 2. (a) Three-dimensional perspective view and (b) cross-sectional view of the air-assisted atomizer. (1) orifice, (2) spring, (3) coil, (4) yoke, (5) fuel inlet, (6) air inlet, (7) needle plug, (8) shell, (9) working gap, and (10) flow diverter.

However, prior research on air-assisted sprays has predominantly concentrated on fundamental characterization of spray characteristics, with limited analysis on the impact of droplets on the turbulence of the jet within the framework of turbulent dispersion multiphase flow.

The primary objective of this paper is to conduct an in-depth analysis of air-assisted spray turbulence characteristics by employing PDPA measurements, with particular attention on the impact of dispersed liquid droplets on the turbulence structure within gas-liquid two-phase jets. The remainder of this paper is structured as follows. A brief introduction to the configuration of droplet-laden jet generation and the measurement facilities is presented in Sec. II. The results of single-phase flow main characteristics and the influence of droplets on gas flow characteristics are presented in Secs. III and Sec IV, respectively. Section V shows the segmental linear relationship between the gas-phase velocity gradient and fluctuation velocity. Conclusions are given in Sec. VI.

II. EXPERIMENTAL CONFIGURATION

A. Spray generation

The principal object of this paper is an air-assisted atomizer, which is a low-pressure, twin-fluid solenoid injector derived from the fuel supply system of aviation heavy fuel unmanned aerial vehicle (UAV) piston engines. This air-assisted atomizer was used to generate droplet-laden jets. Figure 2 shows the three-dimensional (3D) perspective view and cross-sectional view of this atomizer. The mechanical components of the atomizer include a needle plug, shell, yoke, spring, and flow diverter. The energized coil creates an electromagnetic field where the needle plug will be pushed outward by the electromagnetic force to open the nozzle. At this moment, an annular flow channel with a divergent cross-section is generated. After flowing through the nozzle throat, the gas-liquid mixture forms a high-speed two-phase jet and rapidly atomizes to form a droplet-laden flow.

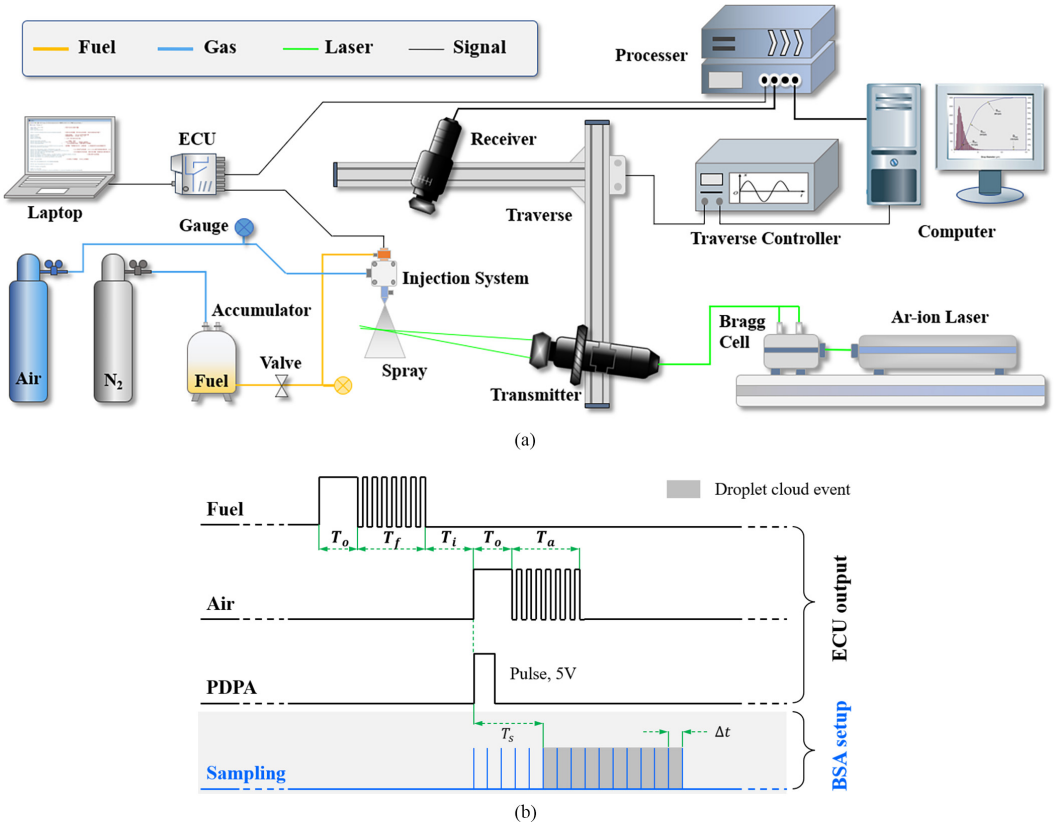

FIG. 3. Experimental setup: (a) phase Doppler particle analyzer (PDPA) and test system components and (b) timing sequence of the injection driving signals.

A self-developed electronic control unit based on a Freescale 16-bit microcontroller MC9S12XDP512 and an Infineon TLE6288 smart multichannel switch was used to output trigger signals for injection and measurement subsystems. A coaxially mounted plain single-hole liquid fuel injector was used to deliver liquid fuel to the air-assisted atomizer, and more specifications about the entire injection system can be found in our previous publications [42,43]. The atomizing gas was supplied by a 40 L compressed air cylinder with a fixed pressure of 8.0 bar. The liquid fuel was supplied by a gas-liquid accumulator, and the pushing gas was provided by a high-pressure nitrogen cylinder to fix the fuel injection pressure of 10 bar.

B. PDPA setup

The measurements of both dispersed (droplet) phase and continuous (gas) phase properties were performed by using phase/Doppler particle analyzer (Dantec Dynamics, FlowExplorer DPSS) in the State Key Laboratory of High Temperature Gas Dynamics of CAS. The PDPA allows the determination of the time-averaged velocities of both phases with a good spatial resolution and the local droplet size distribution [1]. The experimental configuration is shown in Fig. 3(a). The transmitter generated two pairs of laser beams with wavelengths of $\lambda = 561$ nm (yellow light) and $\lambda = 532$ nm (green light). The lens focal lengths of the transmitting and receiving probes were 750 and 1000 mm, respectively. Table I summarizes the relevant optical parameters of the PDPA for both components. The laser transmitter and receiver were oriented at an intersection angle of 33°, which was the second-order refraction angle. The laser Doppler anemometer module was used

TABLE I. Optical parameters of PDPA setup.

Specifications (unit)	Value
Wavelength (nm)	532, 561
Laser beam diameter (mm)	2.6
Beam expander ratio	1
Beam spacing (mm)	60
Fringe spacing (μm)/number	7.116/29
Focal length—transmit (mm)	750
Focal length—receiving (mm)	1000
Scattering angle (deg)	147 (second-order refraction)

to detect droplet velocity, and the scattered yellow laser light was used to measure droplet size. The laser transmitter and receiver were mounted on the traverse arms, whose movements were controlled by the traverse controller. The minimum 3D traversing displacement is 0.1 mm with a regulating accuracy of 0.01 mm. Since, in this paper, we are concerned with intermittent air-assisted spray, PDPA measurements of spray droplets were based on multiple periodic injections to obtain sufficient droplet samples. Therefore, the spray frequency set in this paper is 1 Hz, and the number of injections is set to 40 to collect at least 10 000 samples under every independent operating condition to allow for statistically reliable measurements of the mean and fluctuating velocity components of both phases. The raw PDPA data were postprocessed by MATLAB code. Experiments were performed at ambient pressure of 101 kPa and room temperatures at 20 ± 1 °C.

Figure 3(b) shows the timing sequence of the injection parameter as well as the PDPA trigger. Both events of fuel delivery and air injection are executed by two independent solenoid-driven injectors, each operating with a peak-hold driving current [44,45]. Here, T_o represents the duration for nozzle to open, and T_a and T_f denote the duration to maintain opening status for fuel delivery and air injection, respectively. In this paper, the peak duration was fixed with $T_o = 1.2$ ms, and the hold duration for the air-assisted atomizer was set by $T_a = 1.0$, 2.0, and 3.0 ms. Various hold durations ranging from $T_f = 1.0$ to 9.0 ms for the liquid injector were used to change the injection volume and resultant possible gas-to-liquid ratio for various operating conditions. The fuel-air injection interval was set to $T_i = 0.5$ ms, and the PDPA trigger signal with a pulse duration of 0.2 ms was programmed to synchronize with the air-assisted atomizer trigger signal.

A dense region is usually formed near the nozzle exit, where the high droplet density and large-scale filaments weaken the identification of individual droplets and thus cause a dramatic reduction in sampled droplet numbers [46]. Therefore, the diluted region away from the nozzle exit is usually preferred and often applied by researchers [47,48] to study the fully developed spray, where droplet secondary breakup is completed. Figure 4 depicts the distribution of PDPA measurement points within a half-spray area with the axial direction of x and radial direction of r. A measuring frame (240×96 mm in the x-r plane) oriented perpendicular to the laser was set as $x = 30$ mm axially from the atomizer exit. The measurement points of the PDPA were distributed in this measuring frame with the axial and radial resolution of $dx = 30$ mm and $dr = 6$ mm, respectively. It should be noted that x and r in the following contents are presented as positive values and refer to the axial and radial distance of the measurement point from the nozzle exit, respectively. In addition, the jets are all described in nondimensional form of $x/\Delta L$ and r/d_i in the following context.

In the current experimental configuration, a spatial measurement resolution was chosen that strikes a reasonable balance between retaining as much flow information as possible and managing the measurement workload. As a result, the flow information obtained from current experimental measurements is discrete. To present a visually smooth data trend, the widely used B-spline curves were adopted to fit the discrete data points due to their computational efficiency and compatibility

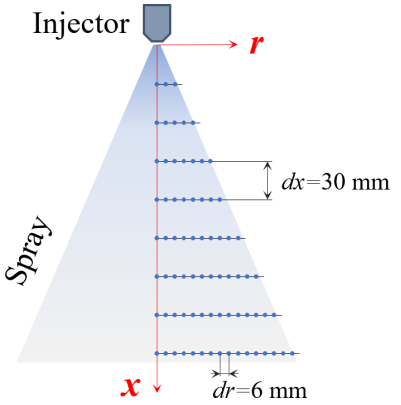

FIG. 4. Locations of phase Doppler particle analyzer (PDPA) scanning and measuring points within the half-spray area. The coordinate system is set up on the central spray axis with the axial direction of x and radial diction of r. Note that both axial and radial locations are presented in nondimensional form when characterizing the jets.

with various regression models. In cases where the data exhibited substantial linear dependence, linear fitting was primarily employed for visualization purposes.

The instrumental error in the droplet measured with the present apparatus does not exceed 3% [49,50]. In addition, to ensure accuracy and reliability, we employed a methodology that involved multiple repetitive injections and a substantial number of droplet samples. This approach allowed us to achieve a high level of repeatability and effectively address any potential errors or uncertainties inherent in the experiments. An uncertainty analysis of the experimental data is incorporated based on the calculation of the standard error (SE), which can be expressed as follows:

$$SE = \pm\sqrt{\frac{\sum_{i=1}^{N}(x_i-\mu)^2}{N(N-1)}}, \tag{2}$$

where N is the number of repeated measurements and x_i is the measurement value for each time. Here, $\mu = \sum_{i=1}^{N} x_i/N$ represents the arithmetic mean value of measurements. The uncertainties of results are presented with an error bar, and the relevant fitting curves are presented with a 95% confidence band, as seen in the following sections.

C. Test conditions

Since, in this paper, we use an integrated solenoid pulse liquid injector to deliver liquid fuel and another solenoid pulse atomizer to generate air-assisted spray, the traditional method of seeding tracer particles to track single-phase jets is not feasible. Based on the effect of fuel-injection duration on the average droplet diameter revealed by authors of previous studies [45], a relatively small fuel-injection duration of $T_f = 1.0$ ms and low-viscosity octane was used to ensure the minimum amount of injected liquid fuel and the smallest possible droplet size. As seen in Fig. 5(a), most of the droplet diameters are <10 μm. Here, $f(D_s)$ represents the probability density function. To ensure a better distinction, the droplets <4 μm in diameter were used as tracer droplets to track the gas phase in both the single- and two-phase flows. The followability examination of droplets with diameters <4 μm for continuous gas-phase flow has been given in the literature [51], and this method has been widely adopted by other researchers [52–55]. Therefore, the gas-phase flow velocity can

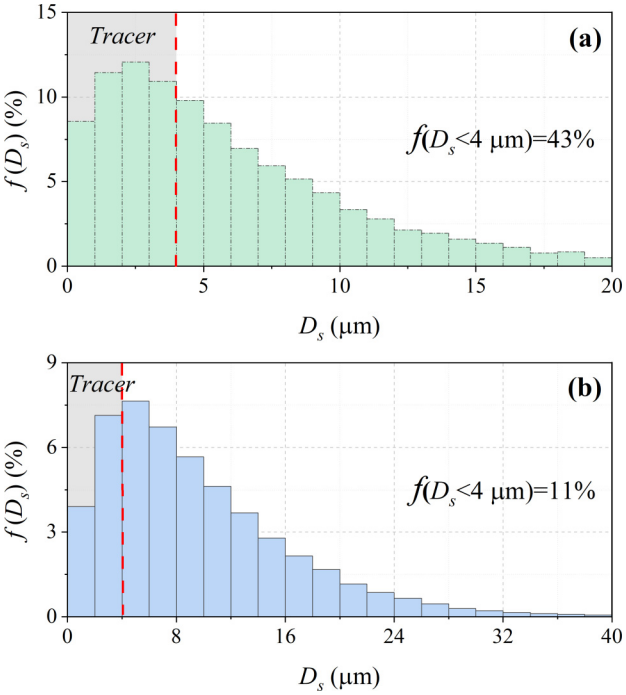

FIG. 5. Droplet diameter distribution of (a) tracer droplets used for single-phase flow measurements at $x/\Delta L = 2$, $r/d_i = 0$, and $T_f = 1.0$ ms using C_8H_{18} and (b) the mixture of the tracer droplets and nontracer droplets measured by PDPA, $x/\Delta L = 2$, $r/d_i = 0$, and $T_f = 3.0$ ms using $C_{12}H_{26}$.

be calculated by $U_g = \overline{U_t}$, here U_t denotes the velocity of tracer droplets. The terminal velocity, relaxation time, and Stokes number of a tracer droplet with the diameter of U_t can be calculated as

$$U_{\text{tem}} = \sqrt{\frac{4gD_t}{3C_d}\left(\frac{\rho_l - \rho_g}{\rho_g}\right)}, \tag{3}$$

$$\tau_0 = \frac{\rho_l D_t^2}{18\mu_g}, \tag{4}$$

$$Stk = \frac{\tau_0}{\tau_t}, \tag{5}$$

where C_d is the drag coefficient, and the dimensionless Stokes number is defined as the ratio of the droplet characteristic time to a flow characteristic time scale.

Due to the prominent turbulent characteristics of the high-speed jet, the characteristic time of the flow is generally characterized by introducing a turbulent time scale as $\tau_t = L/u_r$, where L is the turbulence length scale and u_r is the standard deviation of carrier phase fluctuating velocity. Regarding the length scale, we consider this to be relevant to the object we focus on. Longmire and Eaton [56] indicated that the local particle dispersion is primarily governed by the large-scale turbulent structure of the gas phase. This concept was subsequently explored and expanded upon in the investigation conducted by of Prevost *et al.* [57]. Therefore, a large eddy length scale and fluctuating velocity are generally used to calculate the characteristic time. Considering the approximate symmetry of the jet, the half-width of the jet/spray (denoted by $r_{1/2}$) has been used to characterize the large turbulence scale in this paper.

TABLE II. Tracer droplet characteristics with a diameter of 4 μm.

Cases	D_t (μm)	U_{tem} (m/s)	τ_0 (ms)	Stk
$T_f = 4.0$ ms, $T_a = 0.5$ ms	4	0.259	0.028	0.052
$T_f = 4.0$ ms, $T_a = 3.0$ ms	4	0.259	0.028	0.070

The tracer droplets with the largest diameter ($D_t = 4$ μm) were evaluated for the above parameters, and the results are listed in Table II. The terminal velocity and relaxation time of the selected maximum tracer droplet are relatively small, showing relatively good suspension capability in the spray field. In addition, the calculated droplet Stokes number is $\ll 1$, indicating that these tracer droplets follow the external gas-phase flow streamlines with perfect advection.

Eight cases with different fuel types, fuel-injection durations, and air-injection durations were measured, as shown in Table III. The RP-3 jet fuel was provided by the State Key Laboratory of High Temperature Gas Dynamics of Institute of Mechanics CAS. At the same time, the relevant single components (from C8 to C14) that constitute RP-3 were also considered in this paper, due to their well-defined physical properties. Since the pulse-type air-assisted atomizer typically remains closed and will only open for several milliseconds before the piston reaches the top dead center of compression stroke in piston engines, the injection times set in this paper are in the magnitude of milliseconds, ranging from 1.0 to 9.0 ms, to align with the diverse operating conditions encountered in actual engines.

Case 0 represents the reference single-phase flow case. Cases 1–3 have the same fuel type and air-injection duration with various fuel-injection durations. Cases 1 and 4–5 have the same injection control parameters but different fuel types. In cases 6–8, only the air-injection durations are changed. It has been stated that the PDPA measurement position starts at $x = 30$ mm. Therefore, the average velocity of the carrier phase can be obtained by integration of mean gas velocity within the spray transverse section as

$$U_{g,\,0}(r) = \frac{2}{R_{\max}} \int_0^{R_{\max}} U_g(r) r dr, \tag{6}$$

where $R_{\max}$ is the half-width of the spray at the starting measurement position.

In addition, the definitions of the relevant parameters within the spray field are given. The nondimensional gas fluctuation velocity is defined as the ratio of the rms of the carrier-phase fluctuation velocity to the average velocity of the cross-section at the starting position, i.e.,

$$u_g'(x, r) = \frac{u_{g,\,\text{rms}}}{U_{g,\,0}}. \tag{7}$$

TABLE III. Test liquid and conditions.

Case	Fuel	T_f (ms)	T_a (ms)	$U_{g,\,0}$ (m/s)
Case 0	C_8H_{18}	1.0	2.0	9.50
Case 1	$C_{12}H_{26}$	3.0	2.0	7.47
Case 2	$C_{12}H_{26}$	7.0	2.0	6.60
Case 3	$C_{12}H_{26}$	9.0	2.0	5.81
Case 4	$C_{10}H_{22}$	3.0	2.0	6.57
Case 5	$C_{14}H_{30}$	3.0	2.0	7.77
Case 6	RP-3	3.0	1.0	6.17
Case 7	RP-3	3.0	2.0	7.39
Case 8	RP-3	3.0	3.0	8.18

The mean velocity gradient is represented by the dimensionless parameter as [58]

$$\varsigma = \frac{d(\overline{U_g}/U_{g,\,0})}{d(r/R_{\max})} = \frac{R_{\max}}{U_{g,\,0}}\frac{d\overline{U_g}}{dr}, \tag{8}$$

where $\overline{U_g}$ is the mean velocity.

III. MAIN CHARACTERISTICS OF SINGLE-PHASE FLOW

According to the analysis of the turbulent free shear flows by Pope [59], the spreading rate S of a round turbulent jet is defined as follows:

$$S \equiv \frac{dr_{1/2}(x)}{dx}, \tag{9}$$

where $r_{1/2}(x)$ represents the half-width of a jet. When considering the virtual origin (denoted by x_0) in an actual turbulent jet, the spreading rate is

$$S = \frac{r_{1/2}(x)}{x - x_0}. \tag{10}$$

Based on the mean axial velocity distribution of the single-phase flow condition, the radial position where axial velocity is zero for different axial measurement sections can be obtained. Then the linear relationship between $r_{1/2}(x)$ and x can be determined. In this paper, the spreading rate for the single-phase flow is 0.14, which closely aligns with the data summarized by Pope [59]. The reason for this slight disparity may be attributed to the fact that our current single-phase jet measurements are obtained by seeding small tracer droplets, which deviates somewhat from a purely single-phase jet.

According to the research of Pope [59] and the specific object of this paper, the velocity-decay constant of the single-phase jet can be determined by plotting the inverse of $U_0(x)$, specifically $U_{g,0}/U_0(x)$, as a function of $x/\Delta L$. Then the variation of the mean velocity along the centerline with respect to axial distance can be expressed by

$$\frac{U_0(x)}{U_{g,0}} = \frac{B}{(x - x_0)/\Delta L}, \tag{11}$$

where $U_0(x)$ is the jet centerline velocity and $U_{g,0}$ is the mean gas velocity within the spray transverse section at $x/\Delta L = 1$. By introducing the jet centerline velocity data from single-phase flow into Eq. (3), it is anticipated that the experimental data lie on a nearly straight line over the $x/\Delta L$ range considered. Through linear regression analysis, the slope of the line can be determined, enabling the calculation of the velocity-decay constant, denoted as B, with a value of 15.6. It is noteworthy that this velocity-decay constant is larger than the value reported by Pope [59]. This disparity can be attributed to utilization of a specialized nozzle featuring an annular exit, as opposed to a conventional circular exit nozzle that generates a standard turbulent round jet.

The jet inlet Reynolds number for single-phase flow is defined as

$$\mathrm{Re}_0 = \frac{\rho_g U_0 D_0}{\mu}, \tag{12}$$

where U_0 is the jet velocity at nozzle exit, and $D_0 = d_i - d_o$ is the characteristic linear dimension for an annular flow area of the current nozzle outlet. To determine the Reynolds number, it is essential to obtain the flow velocity at the nozzle exit. However, due to the presence of dense droplets in the near-nozzle field, the PDPA technique is not capable of accurately measuring the velocity of the carrier phase jet. Therefore, we roughly evaluate the current jet-nozzle velocity based on the flow rate (i.e., $m_g = 3.54$ g/s) of a pure gas jet, which is obtained from previous measurements [43],

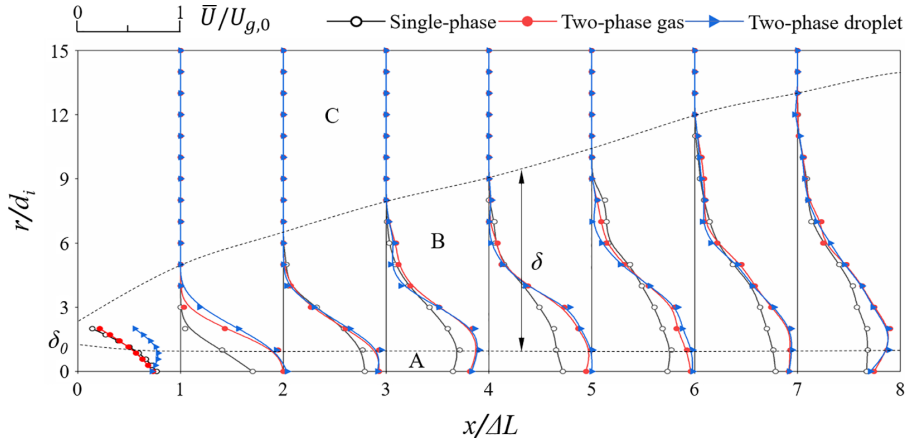

FIG. 6. Mean axial velocity distribution in the two-phase flow for Case 1. Three flow regions are identified: A is the main flow region, B is the shear-layer transition region, and C is the stationary region.

yielding

$$U_0 = \frac{m_g}{\rho_g S_0}, \tag{13}$$

where S_0 is the outlet area. According to the above equation, the calculated jet inlet Reynolds number is $\sim 1.86 \times 10^4$.

IV. INFLUENCE OF DROPLETS ON FLOW FIELD CHARACTERISTICS

Figure 6 shows the mean axial velocity distribution at all the half-spray field measurement sections in the two-phase flow for Case 1. Here, the mean velocity is normalized by the integration of mean gas velocity across the section of $x = 30$ mm. The axial positions are denoted by $x/\Delta L$, where $\Delta L = 30$ mm is the axial distance between measurement sections. The radial positions are expressed as the normalized result of the actual axial position with respect to the inner diameter d_i of the air-assisted atomizer exit. According to the radial distribution of the mean gas-phase velocity, the entire spray field can be divided into three regions, i.e., the main flow region A, the shear-layer transition region B, and the stationary region C. The boundary between regions A and B is the point where the local velocity reaches 95% of the maximum velocity of that section. The boundary between regions B and C represents the radial position where the spray axial velocity reduces to zero (shown by the dashed line). No additional backflow region can be found in region C since the current spray flow is relatively close to a free gas-liquid two-phase jet, which is different from the typical confined expansion flow [25,58]. Therefore, the mean axial velocity in region A (main flow region) is largest while the axial velocity in region C is basically the zero-velocity streamline. The region between A and C is defined as region B, i.e., the shear-layer transition region. The axial velocity difference in this region is significant and has a very steep velocity gradient. The thickness of the shear-layer transition region is denoted by δ. From the comparison of the single- and two-phase jets, one can see that the mean axial velocities of the gas and the droplet of the two-phase jet are approximately the same in the main flow region and the part of the shear-layer transition region close to the main flow region. The mean axial velocities of both the gas and droplets of the two-phase jet are significantly larger than that of the single-phase gas jet, which indicates that the presence of liquid droplets will contribute to the increase of the gas-phase flow velocity in the spray field.

According to Fig. 6, it is evident that the mean axial velocity profiles exhibit a remarkable similarity across different measurement sections, which indicates a potential self-similarity [59].

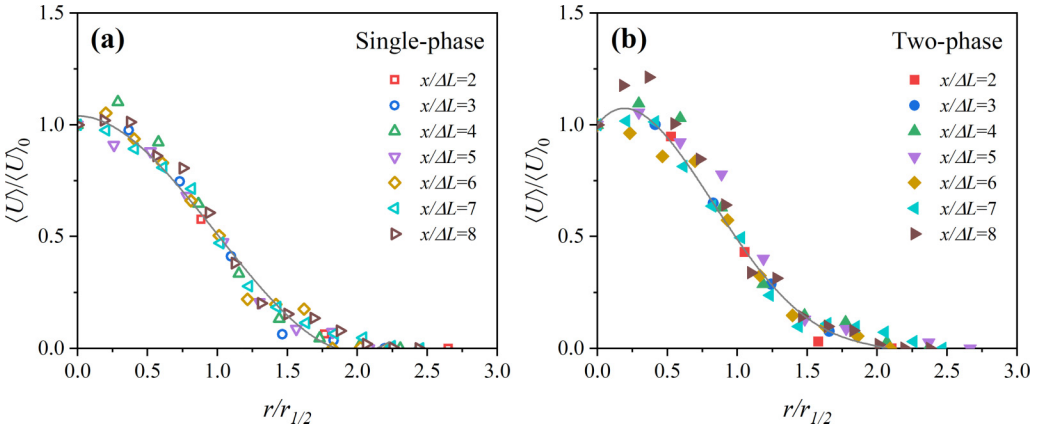

FIG. 7. Mean axial normalized velocity of carrier phase against radial distance: (a) single-phase flow and (b) two-phase flow.

To further investigate this phenomenon, the profiles of $\langle U\rangle/\langle U\rangle_0$ were plotted against $r/r_{1/2}$, and the axial velocity data from different measurement sections collapse onto a single curve, as shown in Fig. 7. In this context, $\langle U\rangle$ refers to the normalized mean velocity $\bar{U}/U_{g,0}$, and $\langle U\rangle_0$ is the normalized mean velocity at the jet centerline ($r = 0$). The half-width of the jet $r_{1/2}$ is defined as the radial distance at which the axial velocity decreases to half of its maximum value [59]:

$$\langle U\rangle(x, r_{1/2}, 0) = \tfrac{1}{2}\langle U\rangle_0(x). \tag{14}$$

It is observed that the mean axial normalized velocity profiles maintain self-similarity for all the cases of single-phase flow although the jet spreads differently at various sections (see Fig. 6). In the case of two-phase flow, the mean axial normalized velocity profiles also demonstrate significant self-similarity. These findings highlight the robustness of the self-similarity phenomenon in both single- and two-phase flows, indicating the presence of underlying mechanisms that govern the flow dynamics. The difference of $\langle U\rangle/\langle U\rangle_0$ between two- and single-phase flow is found in the vicinity of the jet centerline. The $\langle U\rangle/\langle U\rangle_0$ of single-phase flow shows a monotonically decreasing trend with $r/r_{1/2}$. However, $\langle U\rangle/\langle U\rangle_0$ of two-phase flow maintains a roughly constant value when $r/r_{1/2} < 0.25$ and then decreases monotonically with $r/r_{1/2}$. This result is most likely due to the increased jet potential cores caused by the annular exit with a hollow cone geometry of the atomizer nozzle adopted in the experiment.

The fluctuation velocity distributions of the carrier phase at all the measurement sections for single-phase flow (Case 0) and two-phase flow (Case 1) are shown in Fig. 8. One can notice that the gas fluctuation velocities for the two-phase flow are increased at most locations in all the measured sections, which implies turbulence enhancement by the fine droplets. The same result was observed in Ref. [25] but for the region relatively far from the nozzle outlet. In addition, the profile of gas fluctuation velocities for all the measured sections shows a nearly constant and then decreasing function of radial position. Therefore, a moderate fluctuation velocity gradient region (denoted by E), which is close to the spray axis, and a steep fluctuation velocity gradient region (denoted by F), which is far from the spray axis, are identified and defined. A nearly linear relationship between the transition radial position of these two regions and the axial position can be found, as seen in the double dotted line.

Figure 9 illustrates the fluctuation velocity of the carrier phase as a function of radial distance $r/r_{1/2}$. It should be noted that the fluctuation velocity is normalized with the value at the jet centerline. As observed, the fluctuation velocity profiles exhibit significant self-similarity across all measurement sections, regardless of whether it is a single- or two-phase flow. However, a distinct segmented linear relationship between normalized fluctuation velocity and radial distance $r/r_{1/2}$

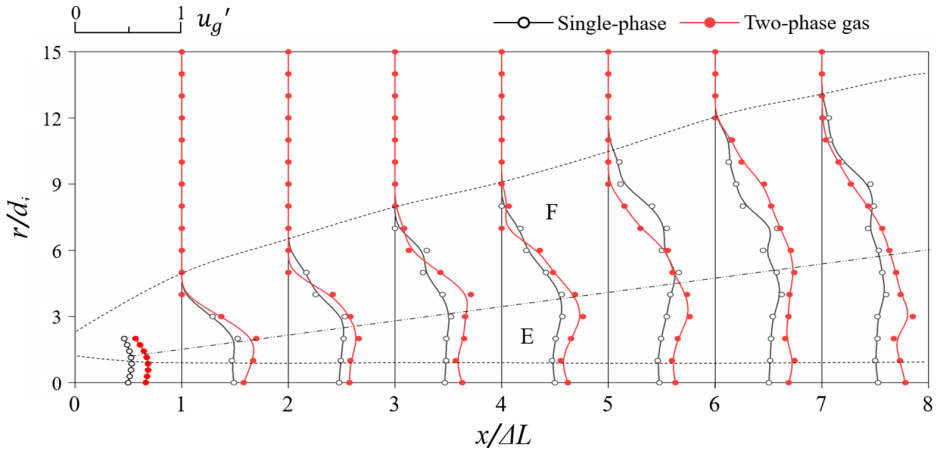

FIG. 8. Carrier phase fluctuation velocity distribution for single-phase flow (Case 0) and two-phase flow (Case 1).

can be observed. This result is consistent with the contents in Sec. V and will be illustrated in more detail in the following context.

The axial velocity gradient distribution of the carrier phase for both single-phase flow (Case 0) and two-phase flow (Case 1) were calculated and are shown in Fig. 10. Significant negative peak values can be found for all measured sections in the single-phase flow, as seen in Fig. 10(a). The peak value decreases as the measured section moves to the far flow field. Moreover, the peak value gradually moves away from the axis ($r/d_i = 0$) as the flow develops. The development of the velocity gradient distribution in the two-phase flow is qualitatively like that in the single-phase flow. However, the peak values of the axial velocity gradient of the carrier phase under the two-phase flow condition are larger than that of the single-phase flow, and the fluctuation of the values is also larger than those of the single-phase flow. This indicates more intense shear for the two-phase flow due to the presence of liquid droplets.

Figure 11 shows the fluctuation velocities of the gas phase under different measurement sections. Different colors are used here to present the moderate (E) and steep (F) fluctuation velocity gradient regions, as illustrated in Fig. 8. A significant linear relation can be found for the gas-phase

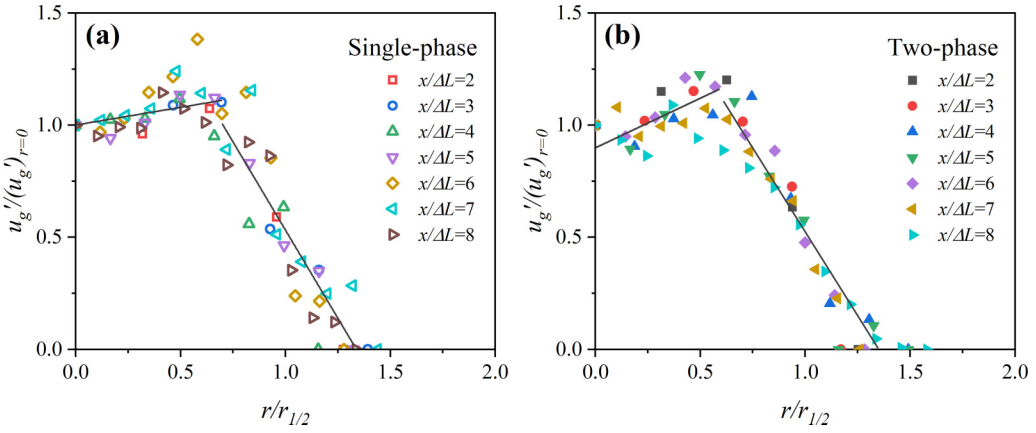

FIG. 9. Fluctuation velocity of carrier phase against radial distance: (a) single-phase flow and (b) two-phase flow.

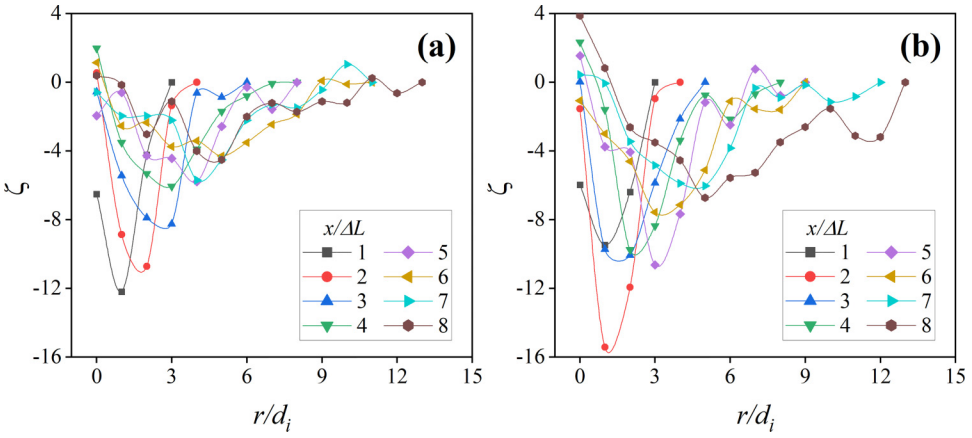

FIG. 10. Variation of the axial velocity gradient of the carrier phase in each measurement section: (a) single-phase flow (Case 0) and (b) two-phase flow (Case 1).

fluctuation velocity as a function of radial positions for region E for both single- and two-phase flows. Here, we define the fluctuation range of u_g' by taking the maximum value of the u_g' difference under different measurement sections as the width of region E. The fluctuation range is denoted by

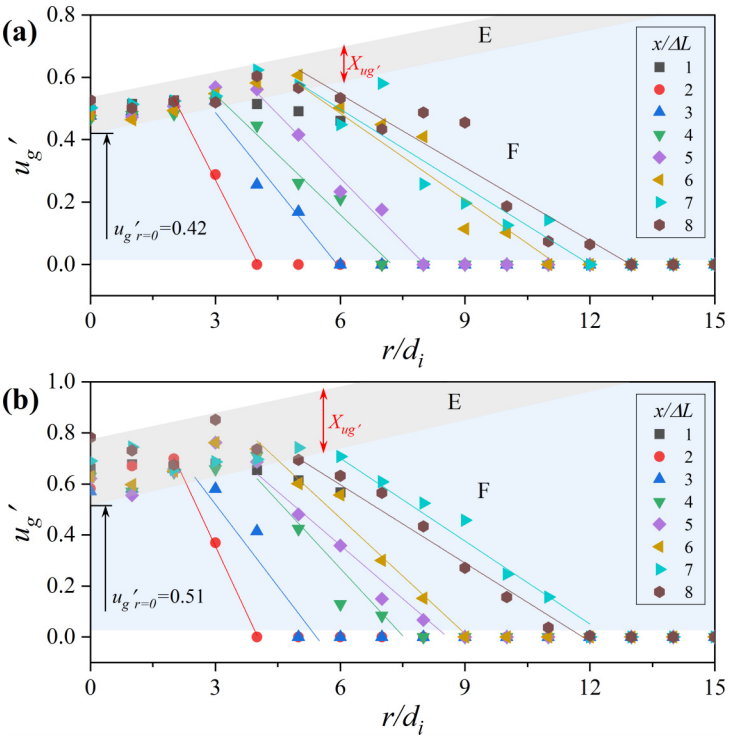

FIG. 11. Variation of gas fluctuation velocities in each measurement section: (a) single-phase flow (Case 0) and (b) two-phase flow (Case 1).

TABLE IV. Comparison of gas fluctuation velocity distribution characteristics.

	$X_{u'_g}$	$u'_{g_{r=0}}$
Single-phase flow	0.11	0.42
Two-phase flow	0.26	0.51

$X_{u'_g}$ and expressed by

$$X_{u'_g} = \max\left[\max\left(u'_{g_j}\right) - \min\left(u'_{g_j}\right)\right]_k. \tag{15}$$

Here, $j = x/\Delta L,\ j \in [1,\ 2, \ldots]$, and $k = r/d_i,\ k \in [1,\ 2, \ldots]$.

The fluctuation range of u'_g (denoted by $X_{u'_g}$) for the two-phase flow is about twice as extended as the single-phase flow, as listed in Table IV. This observation implies turbulence enhancement due to the presence of liquid droplets. In the steep fluctuation velocity gradient region (F), gas fluctuation velocities for both single- and two-phase flows exhibit a linearly decreasing trend with r/d_i. The boundary between regions E and F was fitted to obtain the analytical expression and the intersection with the location of $r/d_i = 0$, as expressed by $u'_{g_{r=0}}$, which represents the initial gas fluctuation velocities of the steep fluctuation velocity gradient region. The $u'_{g_{r=0}}$ of the two-phase flow shows an enhancement of 20% in comparison with the single-phase flow. This result indicates the variation of turbulence between two- and single-phase flows is generated just in the near-nozzle flow area.

The mean axial velocity distribution of the carrier phase for all experimental conditions is shown in Fig. 12. One can see the overall similarity in the profile of mean axial velocity distributions of the carrier phase across various injection durations, test fuels, and air-injection durations. The data in Fig. 12(a) show that the gas velocity of the two-phase flow is all larger than the value of the single-phase flow. In addition, the increase in fuel-injection durations leads to an increase in the mean axial velocity of the carrier phase. Previous researchers [44,51] have revealed that an increase in fuel-injection durations decreases the gas-to-liquid mass ratio of the gas-liquid two-phase jet, which is detrimental to liquid-phase atomization and increases the average droplet size. Therefore, it is concluded that the larger droplet diameter has a positive influence on increasing the average velocity of the carrier phase.

The mean axial velocity distribution of the carrier phase for different test liquid fuels is shown in Fig. 12(b). One can notice that the effect of liquid fuel properties on the mean axial velocity of the carrier phase is not as remarkable as that of fuel-injection durations. This is because twin-fluid sprays are inherently insensitive to the physical properties of the atomized liquid [42,60]. A noteworthy result is that the effect of air-injection duration on the mean axial velocity of the carrier phase is even less significant, as shown in Fig. 12(c). When $r/d_i < 6$, the mean axial velocity of the carrier phase in the mainstream region varies greatly with different air-injection durations. For the positions of $r/d_i > 6$, the mean axial velocity of the carrier phase under different air-injection duration conditions is almost the same. This implies that a potential correlation between liquid-phase and the two-phase flow characteristics can be expected for this investigation.

Since fuel properties and air-injection duration have a relatively small effect on the mean axial velocity of the carrier phase, only the influence of fuel-injection duration is further analyzed here. Figure 13 shows the shear-layer transition region thickness under different working conditions separately, thereby enhancing the clarity of visualization. One can note that the range of δ uncertainty increases with $x/\Delta L$, but the maximum error falls within an acceptable range. As a result, the dependence between δ and $x/\Delta L$ can be established through a linear regression analysis of the data from discrete measurement points.

Additionally, it is not easy to notice the difference between the single- and two-phase flows from the data shown above. Then the results of linear fitting are picked up and presented in another figure for a quantitative comparison, as shown in Fig. 14. The shear-layer thickness of the single-phase

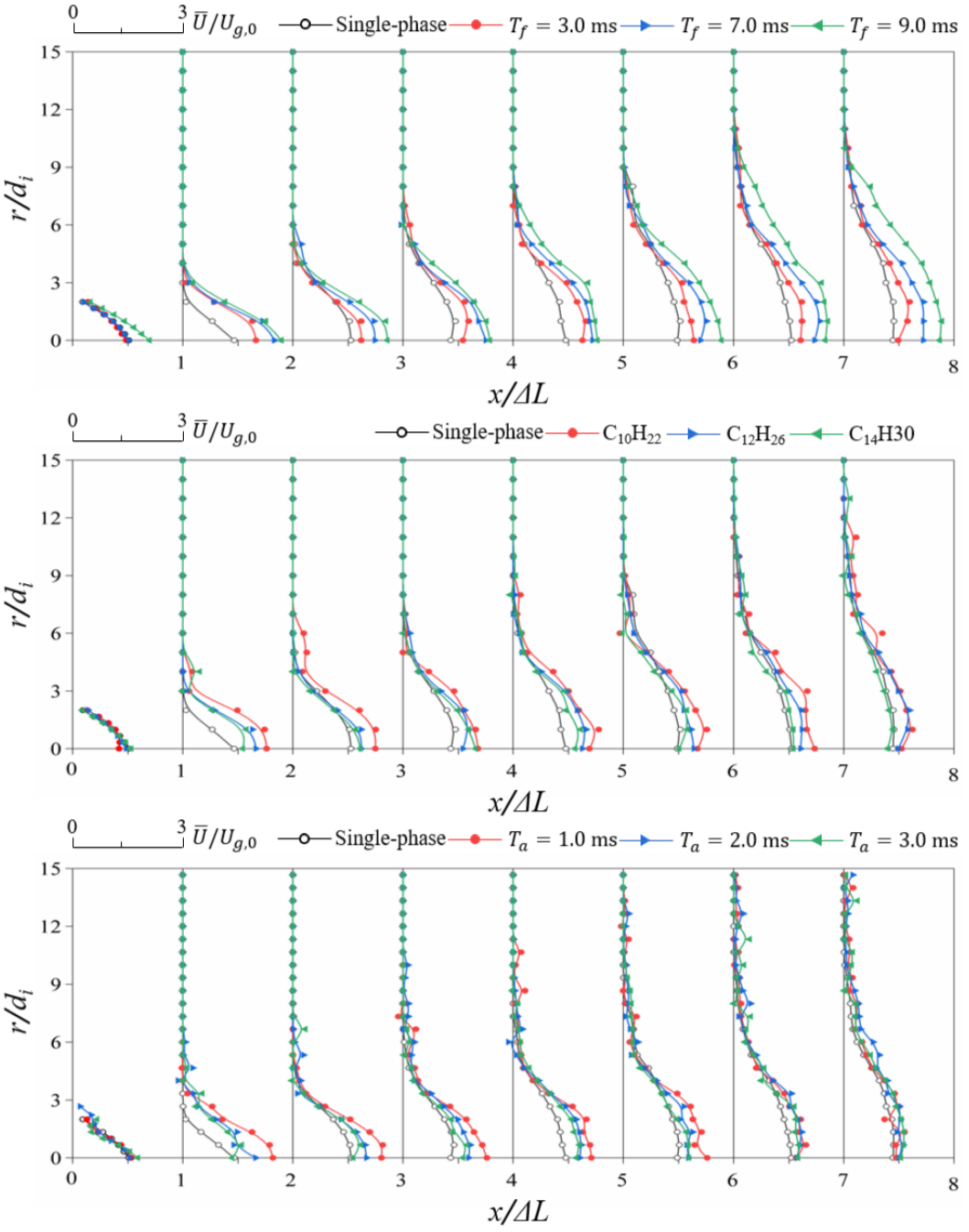

FIG. 12. Mean axial velocity distribution of the carrier phase: (a) different fuel injection durations (Cases 1–3), (b) different test fuel types (Cases 1, 4–5), and (c) different air injection durations (Cases 6–8).

flow shows a steep linear growth function with a significantly larger slope of the fitting curve than that of the two-phase flow. The increasing trend of the shear-layer thickness for the two-phase flow is much flatter. Additionally, the shear-layer thickness for Case 2 ($T_f = 7.0$ ms) is slightly larger than that of Case 1 ($T_f = 3.0$ ms). However, the interesting finding is that the slope of fitting curves

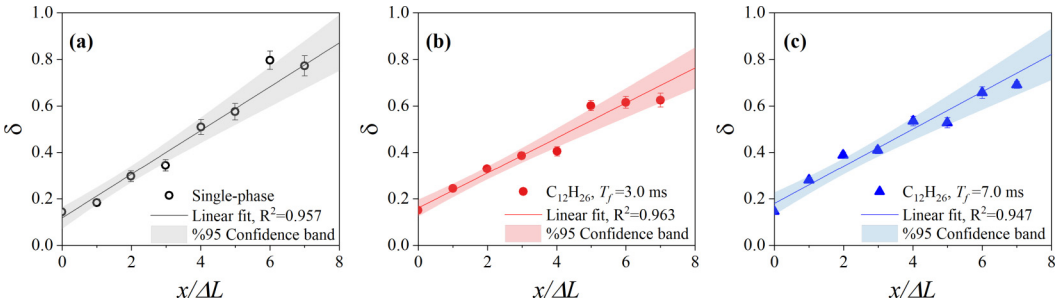

FIG. 13. Shear-layer transition region thickness: (a) single-phase, (b) $T_f = 3.0$ ms (Case 1), and (c) $T_f = 7.0$ ms (Case 2).

of these two cases is nearly the same. The above results indicate that the presence of liquid droplets in the gas-liquid two-phase jet causes axial stretching of the shear-layer transition region of the two-phase flow compared with the single-phase flow, while inhibiting flow dispersion in the radial direction. The consequence is that the shear-layer transition region of the two-phase flow becomes moderately slender compared with that of the single-phase flow. In the current experiments, the gas-liquid jets are generated in a vertical downward direction, and plenty of droplets are dispersed within the carrier phase. Compared with single-phase jets, the droplets and droplet clusters formed due to the inhomogeneity are susceptible to nonnegligible gravitational forces and the resulting axial stretching of the shear-layer region of the gas phase. Under the same conditions, such a droplet gravitational effect is enhanced for larger fuel-injection durations.

The fluctuation velocity distribution of the gas phase for all experimental conditions is shown in Fig. 15. The data show that the increase of fuel-injection duration leads to an increase in the gas-phase fluctuation velocity within the same measurement section, which suggests that larger droplets lead to turbulence enhancement. In addition, some discrepancies can also be noticed when using different liquid fuels. A conservative determination is that u'_g shows an increasing function of the number of carbon atoms in an alkane molecule in the steep fluctuation velocity gradient region. However, no obvious dependence can be found for the region of moderate fluctuation velocity gradient.

A comparison of the gas-phase fluctuation velocity under different air-injection durations reveals that the increase of T_a reduces the fluctuation velocity of the gas phase. This is because, under the

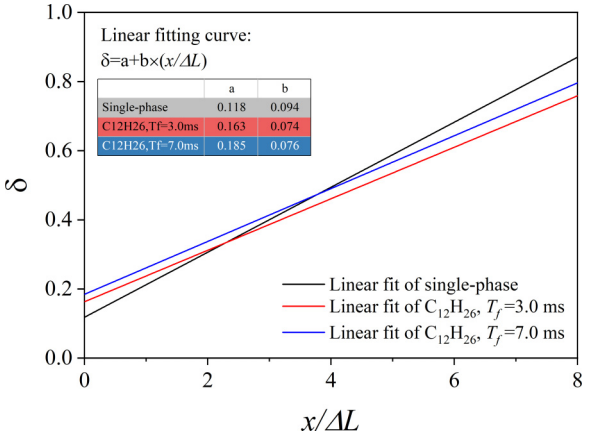

FIG. 14. Shear-layer transition region thickness for different fuel injection durations. $T_f = 3.0$ ms (Case 1) and $T_f = 7.0$ ms (Case 2).

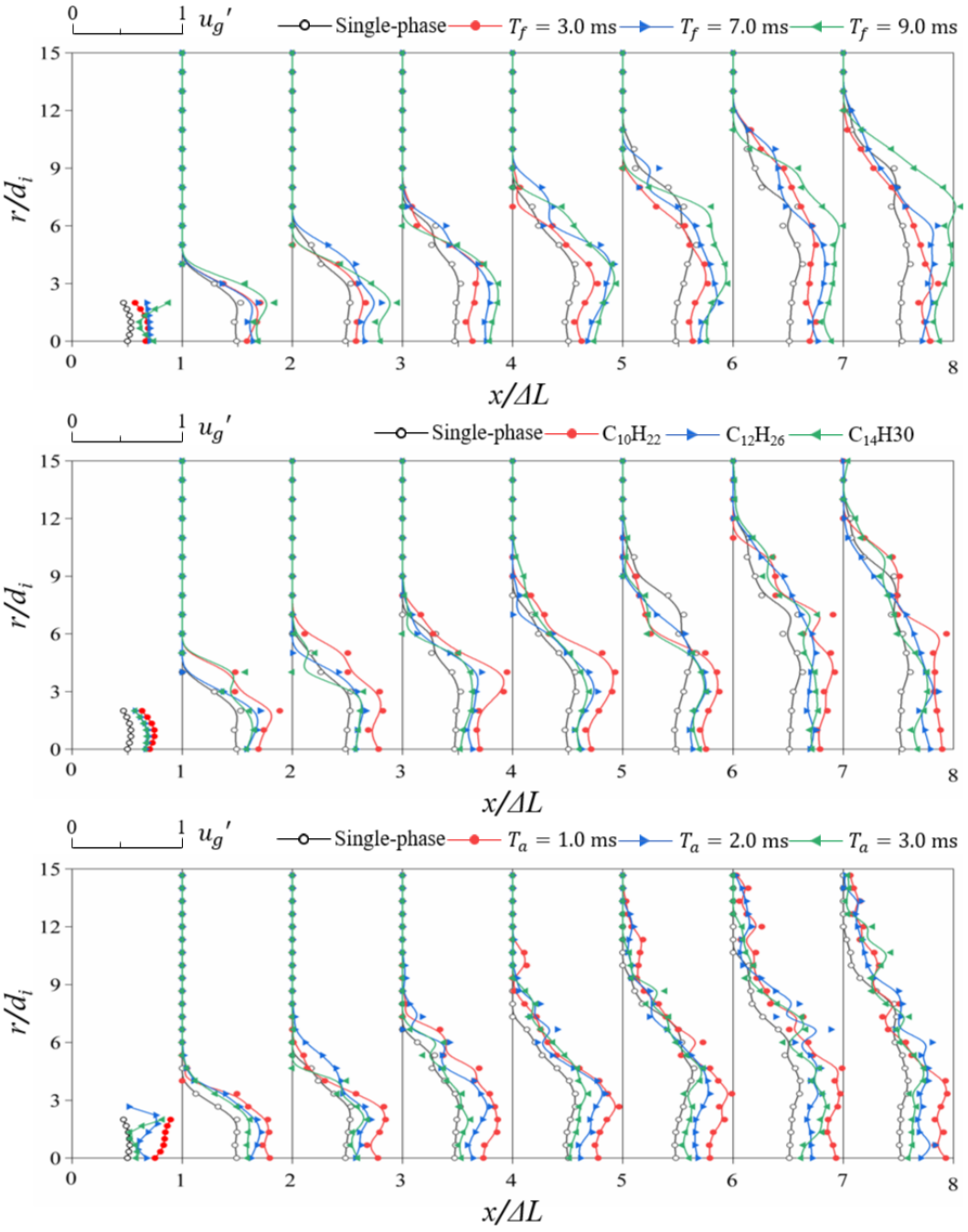

FIG. 15. Fluctuation velocity distribution of the gas phase: (a) different fuel injection durations (Cases 1–3), (b) different test fuel types (Cases 1, 4–5), and (c) different air injection durations (Cases 6–8).

same fuel-injection duration, a larger air-injection duration will lead to an increase in the actual gas-liquid mass ratio, i.e., a decrease in the mass-loading ratio of the gas phase. However, the increase of fuel-injection duration under the same air-injection duration produces the opposite result. Therefore, the effects of both fuel- and air-injection durations on the carrier-phase fluctuation velocity can

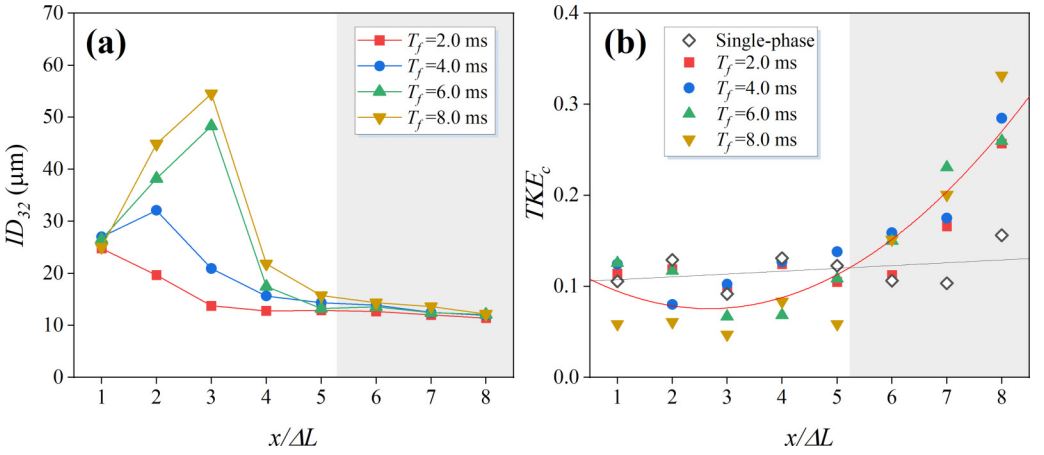

FIG. 16. (a) Integral Sauter mean diameter and (b) turbulent kinetic energy intensity as a function of $x/\Delta L$. Note that the relationship between TKE_c and $x/\Delta L$ is fitted using a simple quadratic polynomial.

be explained by the actual gas-liquid mass ratio. To summarize, the presence of liquid droplets increases the fluctuation velocity of the gas phase, which leads to turbulence enhancement. This effect is enhanced as the gas-liquid mass ratio decreases (by increasing the fuel-injection duration or decreasing the air-injection duration). The above results are consistent with the results of Li *et al.* [25] for the effect of different particle mass-loading ratios on the fluctuation velocity of the gas phase.

Meanwhile, we can notice apparent steep and moderate fluctuation velocity gradient regions from the fluctuation velocity distribution of the gas phase (see Fig. 15) for all current experimental conditions. This result is significantly different from the experimental observations of the gas-phase fluctuation velocity for the gas-solid two-phase shear flows from Ref. [25]. We infer that the gas-phase fluctuation velocity within the flow region remains relatively stable and exhibits a moderate velocity gradient within a certain range near the spray axis and is caused by the annular nozzle exit of the atomizer we used. Compared with the traditional plain-orifice nozzle, which generally produces a jet with a distinct cone structure and a steeper velocity distribution within the jet cross-section, this annular nozzle tends to form a relatively stable fluctuation velocity distribution at the axis of the jet. However, larger fluctuation velocity gradients occur in the region where the spray is close to the external stagnant ambient gas.

The integral Sauter mean diameter (denoted as ID_{32}) is introduced to characterize the mean droplet size for two-phase flow conditions by a single parameter. The simplified equation for the calculation of ID_{32} is [61]

$$\mathrm{ID}_{32} = \frac{\sum_{i=2}^{n} \left(r_i D_{30,i}^3 f_i\right)}{\sum_{i=2}^{n} \left(r_i D_{20,i}^2 f_i\right)}, \tag{16}$$

where ID_{32} represents the whole spray at a certain cross-section perpendicular to the axis of the nozzle exit. Here, $D_{30,i}$ and $D_{20,i}$ are the volumetric and surface diameters, respectively, of droplets measured by using the PDPA at the radial position r_i with droplet arrival frequency of f_i. Also, n is the total number within the measurement section.

Figure 16 shows the overall comparison of the droplet ID_{32} using n-dodecane ($C_{12}H_{26}$) as the test fuel under different fuel-injection durations. The integral Sauter mean diameter increases with the increase of fuel injection duration when $x/\Delta L < 5$. When $x/\Delta L > 5$, ID_{32} remains basically a constant value for different fuel-injection durations.

The turbulent kinetic energy intensity at the position of the spray axis can be calculated as

$$\mathrm{TKE}_c = \frac{u_{gc,\mathrm{rms}}^2}{2U_{gc}^2}, \tag{17}$$

where $u_{gc,\mathrm{rms}}$ and U_{gc} represent gas-phase fluctuation velocity and axial velocity at the spray axis position ($r = 0$), respectively.

Figure 16(b) shows the magnitude of turbulent energy intensity at the spray axis position for different fuel-injection durations. When $x/\Delta L < 5$, the turbulent energy intensity of the single-phase flow is slightly larger than that of the gas-liquid two-phase flow. However, when $x/\Delta L > 5$, the turbulent energy intensity of the single-phase flow is smaller than that of the gas-liquid two-phase flow. The transition position occurs at about $x/\Delta L = 5$, which is consistent with the critical position of the integral Sauter mean diameter of the spray cross-sectional area. Comparing the spray ID_{32} and turbulent energy intensity distributions for both single- and two-phase flows, it is found that larger droplet integration diameters tend to reduce the turbulent energy intensity of the gas phase, while relatively smaller droplet integration diameters tend to increase the turbulent energy intensity of the gas phase. This observation is consistent with the results in the previous discussion on the effect of the presence of droplets in the two-phase flow on the fluctuation velocity of the gas phase.

V. SEGMENTAL LINEAR RELATIONSHIP BETWEEN VELOCITY GRADIENT AND FLUCTUATION VELOCITY

According to the mixing length theory for the single-phase turbulence, it has been established that the local fluctuation velocity is proportional to the velocity gradient [62,63]. Based on this theoretical framework, Li *et al.* [25] examined the relationship between the gas rms fluctuation velocity and the mean velocity gradient for both single- and two-phase flows. They confirmed the anticipated linear relationship between these variables. Furthermore, their results indicated that such a linear relationship exists in all the measured cases. The researchers attributed this observation to the relatively low particle concentration in the measuring scenarios, which was deemed insufficient to significantly influence the turbulence characteristics. Additionally, Tsuji *et al.* [64] showed that the linearity between the fluctuation velocity and the mean axial velocity of the carrier phase can be affected by the particle mass-loading ratio. When the mass-loading ratio is <0.5, the linearity of the carrier phase fluctuation velocity and the mean axial velocity will maintain a more desirable linear relationship. However, the linear relationship between gas fluctuation velocity and the velocity gradient gradually disappears as the particle mass loading >0.5, as seen in Fig. 17.

Our previous measurements [43] with the atomizer (see Fig. 2) showed that, due to the special intermittent injection method, the equivalent liquid droplet mass-loading ratio is ~ 0.6 at the lowest adjustable fuel-injection duration ($T_f = 1.0$ ms, beyond which the nozzle fails to open properly). Therefore, it can be assumed that the gas-phase fluctuation velocity and the mean axial velocity within the current air-assisted spray will not meet the desirable overall linear correlation. In addition, results of flow field characteristics (see Sec. III) have shown that mean velocity gradient of the carrier phase decreases first and then increases with the increase of r/d_i, presenting an obvious nonmonotonic tendency. On the other hand, the fluctuation velocity of the carrier phase first maintains a relatively constant value with the increase of r/d_i and then gradually decreases. As expected, it can be speculated that the fluctuation velocity of the gas phase has no overall satisfactory linearity with respect to the mean velocity gradient.

Hence, the linearity between the fluctuation velocity and velocity gradient in the two regions of moderate and steep fluctuation velocity gradients of the gas phase are tested separately, and the results are shown in Fig. 18. The data in Fig. 18(a) show that u_g' shows a significant linear correlation with the velocity gradient for both single- and two-phase flow conditions. The linearity between scattered data and the fitting curve of the single-phase flow is more favorable than that of

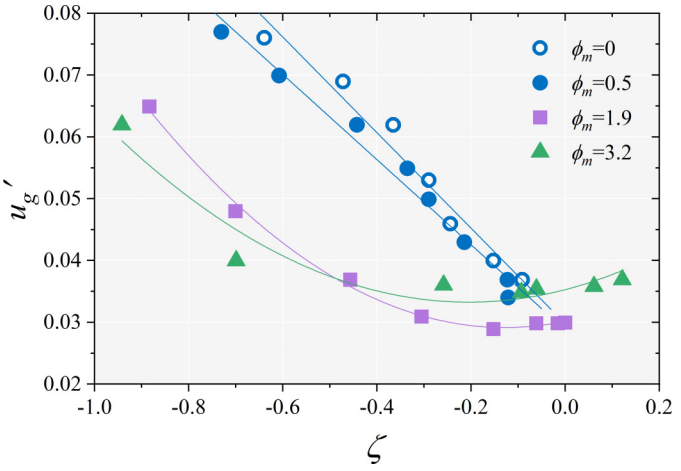

FIG. 17. Relationship between gas fluctuation velocity and mean velocity gradient in vertical gas-solid two-phase flow at different particle mass loading ratios (data from Tsuji *et al.* [64] compiled by Li *et al.* [25]).

the two-phase flow. The only difference is the slope which has a meaning like the mixing length [25]. In the steep fluctuation velocity gradients region, the same results can be found for both single- and two-phase flows. A slight variation is noticed between the two slopes due to the presence of liquid droplets in the two-phase flow.

To present a quantitative comparison between the overall linear correction and our proposed segmented linear relationship for u_g' and ζ, we used Pearson's correlation coefficient to examine their correlation, and the results are presented in the Table V. Here, ρ_E and ρ_F represents Pearson's correlation coefficient for the moderate fluctuation velocity gradient region (E) and the steep fluctuation velocity gradient region (F), respectively. Also, ρ_{all} is Pearson's correlation coefficient when combining these two regions. The results show that Pearson's correlation coefficients for both regions E and F are larger than the values obtained when combining these two regions. Therefore, it can be concluded that the segmented linear correlation is more significant for u_g' and ζ in this paper. This result is mainly due to the escalated mass-loading ratio, which has not been adequately addressed or elucidated in prior investigations.

The correlation between the gas-phase fluctuation velocity and velocity gradient for different axial positions in the moderate fluctuation velocity gradient region is shown in Fig. 19. The selected

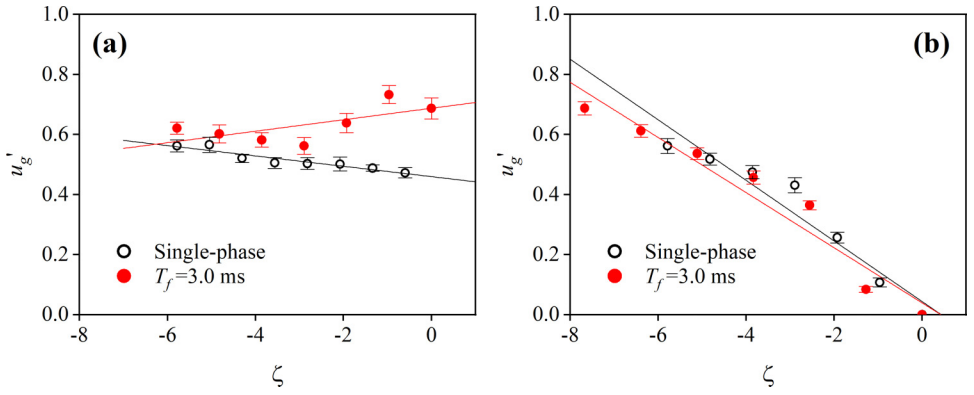

FIG. 18. Relationship between gas fluctuation velocity and mean velocity gradient (Case 1): (a) moderate fluctuation velocity gradient region and (b) steep fluctuation velocity gradient region.

TABLE V. Comparison of Pearson's correlation coefficient.

Case	$x/\Delta L$	ρ_E	ρ_F	ρ_{all}
Case 0	2	0.4505	0.9189	0.3562
	4	0.7201	0.8918	0.5145
	6	0.6763	0.9582	0.4439
	8	0.6159	0.8334	0.4651
Case 1	2	0.8795	0.9182	0.5193
	4	0.4394	0.7397	0.3116
	6	0.7807	0.9332	0.3974
	8	0.4649	0.7936	0.0556

measured sections include $x/\Delta L = 2, 4, 6$, and 8. Note that the selected operating conditions include single- and two-phase flows (Case 1). In general, a relatively pronounced linear correlation can be observed between u_g' and ζ for all concerning conditions. For the position relatively close to the nozzle exit (abef), the slope of the linear fitting function for u_g' and ζ is ∼0, which indicates that the fluctuation velocity of the gas phase hardly changes with the axial velocity gradient. The comparison of single- and two-phase flows shows that the correlation variation of gas-phase fluctuation velocity with velocity gradient is manifested in the position of $x/\Delta L = 8$.

The linear correlation between the fluctuation velocity and velocity gradient of the gas phase at different axial positions in the region of steep fluctuation velocity gradient region is shown in Fig. 20. A negative linear correlation between u_g' and ζ can be found for all selected measurement sections in the steep fluctuation velocity gradient region. This indicates that the fluctuation velocity of the gas phase decreases with the increase of the axial velocity gradient. The slope of the fitting curve of u_g' and ζ for the single-phase flow becomes progressively steeper as the flow develops to the far field. Notable differences between single- and two-phase flows appear in the measurement section of $x/\Delta L = 6$ and 8. The above results indicate that, for the gas-liquid two-phase flow generated by air-assisted spray, the fluctuation velocity of the gas phase in the flow field does not satisfy the overall linear correlation with the velocity gradient within a certain radial direction of the flow cross-section, which is quite different from the previous study [25]. However, for both the moderate and steep fluctuation velocity gradient regions, which are divided according to the gradient

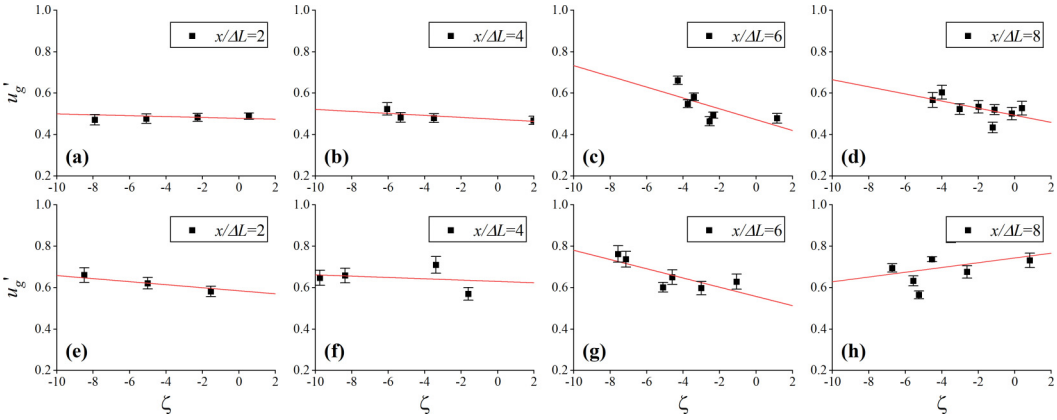

FIG. 19. Correlation of gas-phase fluctuation velocity with velocity gradient at different measurement sections in the moderate fluctuation velocity gradient region: (a)–(d) single-phase flow and (e)–(h) two-phase flow (Case 1).

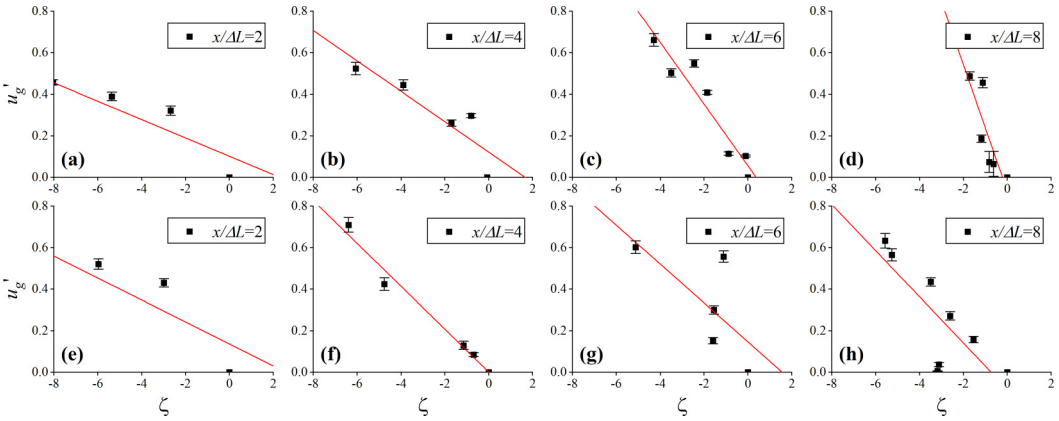

FIG. 20. Correlation of gas-phase fluctuation velocity with velocity gradient at different measurement sections in the steep fluctuation velocity gradient region: (a)–(d) single-phase flow and (e)–(h) two-phase flow (Case 1).

difference of the fluctuation velocity (see Fig. 8), an obvious segmental linear correlation is found between u_g' and ζ.

VI. CONCLUSIONS

In this paper, the gas-phase turbulence modulations of air-assisted spray were studied experimentally under different conditions. The mean and fluctuation velocities were measured using the phase/Doppler particle analyzer, for both the gas phase and liquid droplet phase. The major findings are summarized as follows.

Based on the radial distribution of the mean gas-phase velocity, the droplet-laden flow generated by the air-assisted spray consists of a central main flow region, a shear-layer transition region, and a stationary region. The fluctuation velocity distributions of the carrier phase show a moderate fluctuation velocity gradient region which is close to spray axis and a steep fluctuation velocity gradient region which is far from spray axis, which are identified and defined. The presence of liquid droplets contributes to the increase of gas-phase flow velocity in the spray field.

The effect of liquid droplets on gas-phase turbulence is demonstrated by three aspects: (a) The presence of droplets leads to the increase of fluctuation velocity of gas-phase flow. (b) The fluctuation range of gas-phase fluctuation velocity for the two-phase flow is about twice as extended as the single-phase flow. The initial gas fluctuation velocities of the steep fluctuation velocity gradient region of the two-phase flow show an enhancement of 20% in comparison with the single-phase flow. (c) The presence of droplets causes axial stretching in the shear region of the gas phase, and this stretching effect due to droplet gravity is more pronounced for larger fuel-injection durations.

According to the divided moderate and steep fluctuation velocity gradient regions, a segmental linear relationship between velocity gradient and fluctuation velocity within the two-phase flow field is revealed. This result is different from the assumption of the classical mixing length theory proposed by Prandtl [62], which suggests that the fluctuation velocity of single-phase turbulence is proportional to the velocity gradient.

This experimental investigation was conducted to collect detailed droplet information in air-assisted sprays as well as nominally gas-liquid two-phase jets to evaluate the effect of droplets on gas flow characteristics and to provide a dataset suitable for model validation with the Eulerian-Lagrangian framework.

The data that support the findings of this paper are available from the corresponding author upon reasonable request.

ACKNOWLEDGMENTS

The authors would like to acknowledge the research grant received from the National Natural Science Foundation of China (Grants No. 12072194 and No. 51806013), foundation research funds of the Ministry of Industry and Information Technology (Grant No. JCKY2019602D018), and Beijing Institute of Technology Research Fund Program for Young Scholars (Grant No. 2020CX04047). In addition, the authors appreciate the experimental facilities and necessary help provided by the State Key Laboratory of High Temperature Gas Dynamics of the Institute of Mechanics (CAS).

The authors have no conflicts to disclose.

[1] M. Mergheni, J. Sautet, G. Godard, H. B. Ticha, and S. B. Nasrallah, Experimental investigation of turbulence modulation in particle-laden coaxial jets by phase Doppler anemometry, Exp. Therm. Fluid Sci. **33**, 517 (2009).

[2] S. Elghobashi, Direct numerical simulation of turbulent flows laden with droplets or bubbles, Annu. Rev. Fluid Mech. **51**, 217 (2019).

[3] S. Balachandar and J. K. Eaton, Turbulent dispersed multiphase flow, Annu. Rev. Fluid Mech. **42**, 111 (2010).

[4] L. Brandt and F. Coletti, Particle-laden turbulence: Progress and perspectives, Annu. Rev. Fluid Mech. **54**, 159 (2022).

[5] G. Gai, A. Hadjadj, S. Kudriakov, and O. Thomine, Particles-induced turbulence: A critical review of physical concepts, numerical modelings and experimental investigations, Theor. Appl. Mech. Lett. **10**, 241 (2020).

[6] S. Elghobashi and G. Truesdell, On the two-way interaction between homogeneous turbulence and dispersed solid particles. I: Turbulence modification, Phys. Fluids A: Fluid Dyn. **5**, 1790 (1993).

[7] R. Gore and C. T. Crowe, Effect of particle size on modulating turbulent intensity, Int. J. Multiphase Flow **15**, 279 (1989).

[8] A. D. Paris, Turbulence attenuation in a particle-laden channel flow, Ph.D. thesis, Stanford University, 2001.

[9] H. Sheen, B. Jou, and Y. Lee, Effect of particle size on a two-phase turbulent jet, Exp. Therm. Fluid Sci. **8**, 315 (1994).

[10] Y. Tsuji, Y. Morikawa, T. Tanaka, K. Karimine, and S. Nishida, Measurement of an axisymmetric jet laden with coarse particles, Int. J. Multiphase Flow **14**, 565 (1988).

[11] G. Hetsroni, Particles-turbulence interaction, Int. J. Multiphase Flow **15**, 735 (1989).

[12] A. Ferrante and S. Elghobashi, On the physical mechanisms of two-way coupling in particle-laden isotropic turbulence, Phys. Fluids **15**, 315 (2003).

[13] G. Hetsroni and M. Sokolov, Distribution of mass, velocity, and intensity of turbulence in a two-phase turbulent jet, J. Appl. Mech. **38**, 315 (1971).

[14] K. Luo, J. Fan, and K. Cen, Modulations on turbulent characteristics by dispersed particles in gas-solid jets, Proc. R. Soc. A **461**, 3279 (2005).

[15] T. Tanaka and J. K. Eaton, Classification of Turbulence Modification by Dispersed Spheres Using a Novel Dimensionless Number, Phys. Rev. Lett. **101**, 114502 (2008).

[16] H. Zhou, E. R. Hawkes, T. C. Lau, R. Chin, G. J. Nathan, and H. Wang, Understanding of turbulence modulation and particle response in a particle-laden jet from direct numerical simulations, J. Fluid Mech. **950**, A3 (2022).

[17] P. Gualtieri, F. Battista, and C. Casciola, Turbulence modulation in heavy-loaded suspensions of tiny particles, Phys. Rev. Fluids **2**, 034304 (2017).

[18] J. K. Eaton, Experiments and simulations on turbulence modification by dispersed particles, Appl. Mech. Rev. **47**, S44 (1994).
[19] Y. Liu, L. Jiang, and Y. Zhang, Hydrodynamic modeling of turbulence modulation by particles in a swirling gas-particle two-phase flow, ACS Omega **6**, 10106 (2021).
[20] S. Elghobashi, On predicting particle-laden turbulent flows, Appl. Sci. Res. **52**, 309 (1994).
[21] M. E. Lozier, F. O. Thomas, and S. Gordeyev, PIV investigation of the turbulent boundary layer response to active control actuator, in *AIAA Scitech 2022 Forum* (AIAA, Reston, VA, 2022), p. 0053.
[22] J. Sun, T. Gao, Y. Fan, W. Chen, and R. Xuan, The modulation of particles on coherent structure of turbulent boundary layer in dilute liquid-solid two-phase flow with PIV, Powder Technol. **344**, 883 (2019).
[23] J. D. Kulick, J. R. Fessler, and J. K. Eaton, Particle response and turbulence modification in fully developed channel flow, J. Fluid Mech. **277**, 109 (1994).
[24] D. Mora, A. Cartellier, and M. Obligado, Experimental estimation of turbulence modification by inertial particles at moderate Re λ, Phys. Rev. Fluids **4**, 074309 (2019).
[25] F. Li, H. Qi, and C. You, Phase Doppler anemometry measurements and analysis of turbulence modulation in dilute gas-solid two-phase shear flows, J. Fluid Mech. **663**, 434 (2010).
[26] D. Modarress, H. Tan, and S. Elghobashi, Two-component LDA measurement in a two-phase turbulent jet, AIAA J. **22**, 624 (1984).
[27] Z. Yuan and E. Michaelides, Turbulence modulation in particulate flows—A theoretical approach, Int. J. Multiphase Flow **18**, 779 (1992).
[28] H. Tashiro, E. Watanabe, H. Shinano, K. Funatsu, and Y. Tomita, Effect of mixing gas–fine particle suspension flow with small amount of coarse ones in a horizontal pipe, Int. J. Multiphase Flow **27**, 2001 (2001).
[29] J. Kussin and M. Sommerfeld, Experimental studies on particle behaviour and turbulence modification in horizontal channel flow with different wall roughness, Exp. Fluids **33**, 143 (2002).
[30] R. Clift, J. R. Grace, and M. E. Weber, *Bubbles, Drops, and Particles* (Dover Publications, Inc., Mineola, 2005).
[31] Y. Yamamoto, M. Potthoff, T. Tanaka, T. Kajishima, and Y. Tsuji, Large-eddy simulation of turbulent gas–particle flow in a vertical channel: Effect of considering inter-particle collisions, J. Fluid Mech. **442**, 303 (2001).
[32] M. Fistler, A. Kerstein, S. Wunsch, and M. Oevermann, Turbulence modulation in particle-laden stationary homogeneous shear turbulence using one-dimensional turbulence, Phys. Rev. Fluids **5**, 124303 (2020).
[33] Z. Zuo, T. Fang, H. Wu, and Z. Zhang, High-resolution reconstruction algorithm for the three-dimensional velocity field produced by atomization of two impinging jets based on deep learning, Phys. Fluids **35**, 063306 (2023).
[34] M. Dodd, Direct numerical simulation of droplet-laden isotropic turbulence, Ph.D. thesis, University of Washington, 2017.
[35] J. Shinjo, J. Xia, and A. Umemura, Droplet/ligament modulation of local small-scale turbulence and scalar mixing in a dense fuel spray, Proc. Combust. Inst. **35**, 1595 (2015).
[36] M. S. Dodd and A. Ferrante, On the interaction of Taylor length scale size droplets and isotropic turbulence, J. Fluid Mech. **806**, 356 (2016).
[37] B. Rosa, J. Pozorski, and L.-P. Wang, Effects of turbulence modulation and gravity on particle collision statistics, Int. J. Multiphase Flow **129**, 103334 (2020).
[38] G. Gai, A. Hadjadj, S. Kudriakov, S. Mimouni, and O. Thomine, Numerical study of spray-induced turbulence using industrial fire-mitigation nozzles, Energies **14**, 1135 (2021).
[39] J. A. García, A. Lozano, J. Alconchel, E. Calvo, F. Barreras, and J. L. Santolaya, Atomization of glycerin with a twin-fluid swirl nozzle, Int. J. Multiphase Flow **92**, 150 (2017).
[40] H. Liu and M. C. Altan, *Science and Engineering of Droplets: Fundamentals and Applications* (Noyes Publication/William Andrew Publishing, LLC, New York, 1999).
[41] H. Wu, Z. Zhang, F. Zhang, and W. L. Roberts, Time-resolved low-pressure air-assisted spray performance and unsteadiness evaluation, Phys. Fluids **35**, 043335 (2023).

[42] H. Wu, F. Zhang, and Z. Zhang, Droplet breakup and coalescence of an internal-mixing twin-fluid spray, Phys. Fluids **33**, 013317 (2021).
[43] H. Wu, F. Zhang, Z. Zhang, and L. Hou, Atomization and droplet dynamics of a gas-liquid two-phase jet under different mass loading ratios, Int. J. Multiphase Flow **151**, 104043 (2022).
[44] H. Gao, F. Zhang, Z. Zhang, S. Wang, and H. Wu, Trajectory deviation of target jet of air-assisted spray under different conditions, Fuel **249**, 252 (2019).
[45] H. Wu, F. Zhang, Z. Zhang, Z. Guo, W. Zhang, and H. Gao, On the role of vortex-ring formation in influencing air-assisted spray characteristics of n-heptane, Fuel **266**, 117044 (2020).
[46] Y. Li, H. Guo, Y. Shen, X. Ma, L. Chen, and L. Feng, Macroscopic and microscopic characteristics of gasoline and butanol spray atomization under elevated ambient pressures, Atomization Sprays **28**, 779 (2018).
[47] C. Liu, K. Wu, Z. Zhang, Y. Yuan, and X. Fan, Experimental study of the spray characteristics of twin-fluid atomization: Focusing on the annular flow regime, Phys. Fluids **34**, 123309 (2022).
[48] M. Liu, Y. Duan, T. Zhang, and Y. Xu, Evaluation of unsteadiness in effervescent sprays by analysis of droplet arrival statistics—The influence of fluids properties and atomizer internal design, Exp. Therm. Fluid Sci. **35**, 190 (2011).
[49] J. Wang, C. Xu, G. Zhou, and Y. Zhang, Spray structure and characteristics of a pressure-swirl dust suppression nozzle using a phase doppler particle analyze, Processes **8**, 1127 (2020).
[50] L. Hou, D. Zhang, and X. Fan, Spatial structure and droplet distribution of atomization by three circularly arranged impinging jets, Atomization Sprays **32**, 29 (2022).
[51] H. Wu, F. Zhang, and Z. Zhang, Fundamental spray characteristics of air-assisted injection system using aviation kerosene, Fuel **286**, 119420 (2021).
[52] J. C. Lasheras, E. Villermaux, and E. J. Hopfinger, Break-up and atomization of a round water jet by a high-speed annular air jet, J. Fluid Mech. **357**, 351 (1998).
[53] V. Ferrand, R. Bazile, J. Borée, and G. Charnay, Gas-droplet turbulent velocity correlations, and two-phase interaction in an axisymmetric jet laden with partly responsive droplets, Int. J. Multiphase Flow **29**, 195 (2003).
[54] J. Jedelsky, M. Maly, N. Pinto del Corral, G. Wigley, L. Janackova, and M. Jicha, Air-liquid interactions in a pressure-swirl spray, Int. J. Heat Mass Trans. **121**, 788 (2018).
[55] M. Manish and S. Sahu, Droplet clustering and local spray unsteadiness in air-assisted sprays, Exp. Therm. Fluid Sci. **100**, 89 (2019).
[56] E. K. Longmire and J. K. Eaton, Structure of a particle-laden round jet, J. Fluid Mech. **236**, 217 (1992).
[57] F. Prevost, J. Boree, H. J. Nuglisch, and G. Charnay, Measurements of fluid/particle correlated motion in the far field of an axisymmetric jet, Int. J. Multiphase Flow **22**, 685 (1996).
[58] L. Fei, H. Qi, and C. You, Analysis of turbulence modulation in a sudden-expansion flow laden with fine particles, AIP Conf. Proc. **914**, 69 (2007).
[59] S. B. Pope, *Turbulent Flows* (Cambridge University Press, Cambridge, 2000).
[60] M. Zaremba, L. Weiß, M. Malý, M. Wensing, J. Jedelský, and M. Jícha, Low-pressure twin-fluid atomization: Effect of mixing process on spray formation, Int. J. Multiphase Flow **89**, 277 (2017).
[61] J. Jedelsky and M. Jicha, Novel modifications of twin-fluid atomizers: Performance, advantages and drawbacks, in *23rd Annual Conference on Liquid Atomization and Spray Systems* (ILASS, Europe, 2010).
[62] L. Prandtl, *Essentials of Fluid Dynamics, with Application to Hydraulics, Aeronautics, Meteorology and Other Subjects* (Hafner Pub., New York, 1954).
[63] L. Yarin and G. Hetsroni, Turbulence intensity in dilute two-phase flows: The particles-turbulence interaction in dilute two-phase flow, Int. J. Multiphase Flow **20**, 27 (1994).
[64] Y. Tsuji, Y. Morikawa, and H. Shiomi, LDV measurements of an air-solid two-phase flow in a vertical pipe, J. Fluid Mech. **139**, 417 (1984).